This is an *Accepted Manuscript*, which has been through the Royal Society of Chemistry peer review process and has been accepted for publication.

Accepted Manuscripts are published online shortly after acceptance, before technical editing, formatting and proof reading. Using this free service, authors can make their results available to the community, in citable form, before we publish the edited article. We will replace this *Accepted Manuscript* with the edited and formatted *Advance Article* as soon as it is available.

You can find more information about *Accepted Manuscripts* in the **Information for Authors**.

Gold nanoparticles-ultrananocrystalline diamond hybrid structured materials for high-performance optoelectronic device applications

Kamatchi Jothiramalingam Sankaran,[a] Srinivasu Kunuku,[b] Balakrishnan Sundaravel,[c] Ping-Yen Hsieh,[a] Huang-Chin Chen,[d] Keh-Chyang Leou,[b] Nyan-Hwa Tai*[a] and I-Nan Lin*[d]

[a]*Department of Materials Science and Engineering, National Tsing Hua University, Hsin-Chu, Taiwan 300, Republic of China.*

Email: nhtai@mx.nthu.edu.tw

[b]*Department of Engineering and System Science, National Tsing Hua University, Hsin-Chu, Taiwan 300, Republic of China.*

[c]*Materials Science Group, Indira Gandhi Centre for Atomic Research, Kalpakkam 603 102, India.*

[d]*Department of Physics, Tamkang University, Tamsui, Taiwan 251, Republic of China.*

Email: inanlin@mail.tku.edu.tw

Hybridization of gold nanoparticles in the ultrananocrystalline diamond materials improves the electrical conductivity of the materials to a high level of 230 $(\Omega \text{ cm})^{-1}$ with sheet carrier concentration of 8.9×10^{20} cm^{-2}. These hybrid materials show enhanced electron field emission (EFE) properties, viz. low turn-on field of 2.1 V/μm with high EFE current density of 5.3 mA/cm^2 (at an applied field of 4.9 V/μm) and life-time stability up to a period of 372 min. The fabrication of these hybrid materials with high conductivity and superior EFE behaviors is a direct and simple process which opens new prospects in flat panel displays and high brightness electron sources.

Keywords: ultrananocrystalline diamond materials, gold nanoparticles, electron field emission, plasma illumination

Combination of two chemically different nanostructured materials to form a hybrid nanomaterial provides a versatile building block for the construction of modern nanodevices. Diverse hybrid nanostructures, comprising metal/metal, metal/semiconductor, metal/magnet, and magnet/semiconductor ones, have been designed.[1–4] Compared with single component ones, hybrid nanostructures can reveal superior properties or new functionalities. Bimetallic nanostructures, like Ag shell/Au nanocrystals[3] and Au/CdSe nanoflowers[4] result in improved chemical stabilities, high catalytic activities and have been utilized for plasmon-enhanced photocatalysis. In metal nanoparticles/carbon based heterostructures, decoration of carbon nanotubes (CNTs) with some metal nanoparticles expands their applications from CNT assisted catalytic systems to complex conductor networks in bioelectronics, broad-band optical emitters, electrodes and catalysts.[5–7] Predominantly, Au nanoparticles are one of the noble metal nanostructures that possess many outstanding material properties such as special optical properties, unusual electronic properties including conductivity by activated electron hopping, and remarkably high catalytic activity.[8] While bulk Au is extremely unreactive and catalytically inactive, Au nanoparticle is capable of catalyzing a wide variety of reactions. These include the oxidation of CO,[9,10] the selective hydrogenation of acetylene,[11] hydrogenation of halogen compounds, reduction of nitrogen oxides and photocatalytic hydrogen production.[12] Particularly, Au has attracted attention as catalyst for nanocarbon materials' growth because semiconductor nanowires could be grown using Au nanoparticles.[13] Au nanoparticles of size less than 50 nm shows extreme catalytic activity on the growth of single walled CNTs (SWNTs)[14] and graphene.[15] This catalytic activity could be due to the solubility of carbon in Au nanoparticles[16] and it is found to be dependent on Au particle size.[17] Being encouraged by a unique possibility to

combine two nanostructured materials, we fabricated novel Au nanoparticles-ultrananocrystalline diamond (UNCD) hybrid structured materials and investigated their electron field emission (EFE) and plasma illumination (PI) properties. Hitherto, the mechanism based on the catalytic activity of Au nanoparticles for the growth of diamond materials as well as the obtained high stability electron field emitting Au-UNCD hybrid structured materials have not been reported.

A simple and practicable method is followed for the fabrication of Au nanoparticles-UNCD hybrid structured materials. First, the UNCD materials with ultra-smooth surface characteristics at nanoscale were grown on Au-coated silicon (Au(Si)) substrates by microwave plasma enhanced chemical vapor deposition (MPECVD) system. Second, 500 keV Au ions with an ion fluence of 1 x 10^{17} ions/cm^2 were implanted on UNCD/Au(Si) materials at room temperature in a pressure below 10^{-7} Torr. Thus obtained materials were designated as "Au-UNCD/Au(Si)" hybrid structured materials. The depth profiles of Au-UNCD/Au(Si) hybrid structured materials are examined using secondary ions mass spectroscopy (SIMS) so as to understand the behavior of Au in the UNCD materials. Fig. 1(a) shows SIMS depth profiles of Au-UNCD/Au(Si) hybrid structured materials, revealing the presence of Au-ion counts to a depth of about 230 nm due to implanted Au ions (region I), confirming that Au ions have been confined in the UNCD materials. The Au peak around 230 nm is nearly twice that of the projected range of 500 keV Au ions, which can be ascribed to the presence of abundant grain boundaries of less dense than the crystalline diamond materials. The radiation enhanced diffusion of implanted ions might also be a factor for such a phenomenon.[18] SIMS profiles reveal another Au peak near the Si-to-diamond interface region, which contains two interdiffusion

regions: (i) region II, where the Si and Au species decreased rapidly away from the interface to the surface of diamond materials, and (ii) region III, where Au interacted with the Si and the carbon species in a complicated way.

The featured Au-UNCD/Au(Si) structured materials were subjected to Hall measurements with the measuring probes directly in contact with the materials. The Hall measurements for the UNCD materials directly grown on Si (UNCD/Si) was also measured for comparison. Interestingly, the Au-UNCD/Au(Si) hybrid structured materials exhibit high electrical conductivity of $\sigma = 230$ $(\Omega \text{ cm})^{-1}$ with sheet carrier concentration of $n_e = 8.9 \times 10^{20}$ cm^{-2} and mobility of $\mu_e = 1.2 \times 10^3$ $\text{cm}^2/\text{V} \cdot \text{s}$. In contrast, the resistivity of the UNCD/Si materials is too large to be measurable by van der Pauw configuration. The electronic parameters (σ, n_e and μ_e) related to Au-UNCD/Au(Si) hybrid structured materials are better than those for the conducting UNCD materials ever reported.[19–23] (cf. Table 1).

It should be noted that the utilization of Au-coating on Si substrates is to suppress the formation of amorphous carbon (*a-C*) interlayer and to enhance the transport efficiency of electrons crossing the diamond-to-Si interface. When the UNCD materials were grown directly on Si substrates, the interdiffusion between C and Si species usually does not occur, which is illustrated in Fig. S1 of the supporting information. The nucleation of diamond requires a transition layer, which is *a-C*. Such a phenomenon is illustrated by transmission electron microscopy (TEM) micrograph in Fig. S2 of the supporting information. The *a-C* interlayer is relatively resistive and will markedly hinder the transport of electrons crossing the diamond-to-Si interface. The SIMS profiles confirm that the presence of Au-coating efficiently induced the

interdiffusion between diamond, Au and Si materials (cf. Fig. 1(a)). However, the effectiveness in enhancing the electron transport crossing the diamond-to-Si interface due to the utilization of Au-coating needs to be confirmed. For this purpose, the surface and the interface electron transport properties of the Au-UNCD/Au(Si) hybrid structured materials were characterized by a four-probe technique. Inset in Fig. 1(b) shows the measurements with all of the four probes placed on the same surface of the diamond materials, which measured the resistance along the surface of the films (designated as surface resistance). The surface resistance of the Au-UNCD/Au(Si) materials is 66 Ω (curve II, Fig. 1(b)), whereas those of the UNCD/Si materials is 4250 Ω (curve I, Fig. 1(b)) that is in accord with the Hall measurements. Moreover, Fig. 1(c) shows the I-V characteristics with the four probes arranged across the interface, as in the configuration shown in the inset of Fig. 1(c), which measured the resistance crossing the diamond-to-Si interface (designated as interface resistance). This figure reveals that the UNCD-to-substrate interface resistance is around 41 Ω for Au-UNCD/Au(Si) materials (curve II, Fig. 1(c)), which is markedly lower than the interface resistance for UNCD/Si materials (6.8 x 10^4 Ω; curve I, Fig. 1(c)).

The EFE behaviors of these highly conducting Au-UNCD/Au(Si) hybrid structured materials are depicted in Fig. 1(d), which demonstrates that these materials possess admirable field emission properties. The EFE parameters were extracted from the obtained I-V curves by using the Fowler-Nordheim (F-N) equation:[24]

$$J\mathrm{e} = \left(\frac{A\beta^2 E^2}{\varphi}\right)\exp\left(-\frac{B\phi^{\frac{3}{2}}}{\beta E}\right) \tag{1}$$

where $A = 1.54 \times 10^{-6}$ A eV/V^2 and $B = 6.83 \times 10^9$ eV$^{-3/2}$ V/m, β is the field-enhancement factor, J_e is the EFE current density, E is the applied field and φ is the work function of the emitting materials. The plot of EFE current density versus applied electric field (J_e-E) shows a considerably low turn-on field of E_0=2.6 V/μm (defined at a J_e of 10 μA/cm^2) with comparatively high EFE current density of 5.3 mA/cm^2 at the applied field of 4.97 V/μm for Au-UNCD/Au(Si) materials (curve II, Fig. 1(d)). Such an EFE behavior is markedly superior to those of the UNCD/Si materials, which possess an E_0 value of 19.3 V/μm with J_e value of 1.03 mA/cm^2 (at the applied field of 33.3 V/μm) (curve I, Fig. 1(d)). Additionally, the effective work functions of these UNCD materials calculated from the slope of the F-N plots (Fig. S3, Supporting Information) are $(\varphi_{eff})_{\text{Au-UNCD/Au(Si)}}$ = 0.0132 eV and $(\varphi_{eff})_{\text{UNCD/Si}}$ = 0.0194 eV. Consequently, the Au-UNCD/Au(Si) materials own lower work function for electron emission and thus exhibit far more efficient EFE behavior, viz. lower E_0 and higher J_e values as compared with the other conducting UNCD field emitters[19–23] that are summarized in Table 1. Moreover, the life-time stability measurements for these materials have been carried out, because the stability of the field emission current is an important parameter related to prospective applications of cold cathode materials. The corresponding J_e versus time curve is shown as inset of Fig. 1(d), indicating the emission current variations recorded over a period of 372 min at a working field of 4.38 V/μm, corresponding to J_e of 2.3 mA/cm^2, for Au-UNCD/Au(Si) materials (curve II, inset of Fig. 1(d)). As seen from the figure, no significant discharges or spikes due to emitter adsorbates are produced and the emitted current remains constant over this period of time. Conversely, UNCD/Si materials show the life-time stability only up to a period of 246 min at a working field of 28.5 V/μm corresponding to J_e of 0.20 mA/cm^2 (curve I, inset of Fig. 1(d)).

The intriguing phenomena in the robustness of the Au-UNCD/Au(Si) materials can be better illustrated by using these EFE emitters as cathodes for a microplasma device, which is the harshest environment for electron emitters, as the emitters are subjected to energetic Ar-ions bombardment in these devices. Generally, the microplasma based devices represent a photonics technology at the intersection of plasma science, optoelectronics and materials science and provide a great potential for a broad spectrum of applications in microdisplays, material synthesis and elemental analysis.[25,26] Particularly, diamond materials exhibits a large secondary electron emission efficiency (γ-coefficient), which is especially proficient for serving as a cathode material in microplasma based devices.[27,28] Fig. 1(e) shows that the microplasma devices using Au-UNCD/Au(Si) materials as cathode exhibit superior plasma image than those using UNCD/Si as cathodes. The microplasma devices using the Au-UNCD/Au(Si) materials as cathode can be triggered by a voltage as low as 350 V (image series II). In contrast, the UNCD/Si based microplasma devices need higher voltage, around 370 V (image series I), to trigger the plasma. The intensity of the plasma increases monotonically with the applied voltage. The superior PI characteristics are better illustrated by the variation of the plasma density (n_p) versus the applied field. Notably, the plasma density (n_p) was estimated from the plasma current density (J_p) (see Fig. S4 and the detail procedure for the evaluation of plasma density from plasma current density in supporting information). Fig. 1(f) indicates that the plasma density (n_p) increased monotonously with the applied voltage and reached $n_p=1.5 \times 10^{17}$ cm^{-3}, at an applied voltage of 520 V, for Au-UNCD/Au(Si) materials based microplasma devices (curve II), whereas it achieved only $n_p=0.92 \times 10^{17}$ cm^{-3} for UNCD/Si based ones (curve I).

7

To evaluate the stability of the PI behavior from Au-UNCD/Au(Si) based microplasma devices, the plasma current was monitored over a long period with a constant applied voltage of 450 V. The PI intensity of the Au-UNCD/Au(Si) based microplasma devices remains stable over 25655 s (7.12 h) and the plasma current density of 1.90 mA/cm^2 is upheld for this period, showing high stability of the Au-UNCD/Au(Si) materials (curve II, inset of Fig. 1(f)). In contrast, the J_p value of 1.52 mA/cm^2 decreased fast after 13027 s (3.62 h) of plasma ignition for the UNCD/Si-based microplasma devices (curve I, inset of Fig. 1(f)). It should be mentioned that the life-time PI measurement shown in the inset of Fig. 1(f) was preceded under rather high applied voltage, i.e., 450 V. In this measurement, the cathode was bombarded continuously by Ar-ions of rather high kinetic energy, i.e., 450 eV. The cathode materials are expected to experience high erosion rate. In practical application, the cathode-to-anode voltage will be lowered markedly (e.g. < 200 V) so as to reduce the kinetic energy of Ar-ions, bombarding the cathode, that will lower the erosion rate for the cathode materials and increase the life-time (the cathode-to-anode separation will usually be decreased to maintain the electric field). However, in this case, the life-time will be too long to be measurable in reasonable time scale for comparing the performance of the two cathode materials. Apparently, the better illumination performance of the microplasma devices based on the Au-UNCD/Au(Si) materials, as compared with those of bare UNCD/Si-based ones, is closely correlated with the superior EFE properties of the Au-UNCD/Au(Si) materials.

To elucidate the basis of enhancement of the EFE and the PI performances of highly conducting Au-UNCD/Au(Si) materials, the microstructure of these materials was examined using TEM (JEOL-2100F, 200 eV). Fig. 2(a) shows the typical cross-sectional bright field (BF)

TEM micrograph of Au-UNCD/Au(Si) materials, in which the Au-ion implanted and the Au-interlayer regions are clearly marked. The inset in Fig. 2(a) reveals that the selective area electron diffraction (SAED) pattern contains mainly the ring shaped pattern, corresponding to diamond (111), (220) and (311) lattice planes, which implies that most of the materials contain randomly oriented nano-sized diamond grains. There exists a weak extra diffraction ring inside the diamond ring, which corresponds to Au material. In addition, a prominent diffused ring in the center of this SAED indicates the presence of some sp^2-bonded carbon phases in these hybrid materials. Moreover, there appears a very faint diffraction spots located in between Au-ring and central diffuse rings that corresponds to SiC phase. The significance of the occurrence of SiC phase will be discussed later.

More detailed investigations were carried out on the identification of different phase constituents in Au-UNCD/Au(Si) materials by high resolution TEM (HRTEM) studies. Fig. 2(b) shows the structure image obtained from Au-ion implanted region of Au-UNCD/Au(Si) materials (designated as A, Fig. 2(a)). We observe that there are Au nanoparticles of size around 2−5 nm (highlighted as Au in Fig. 2(b)) evenly dispersed among the matrix of ultra-small diamond grains in this region. Fourier-transformed (FT) diffractogram image of the whole structure image (FT_{0b}) shows that, besides a spotted diamond diffraction pattern arranged in a ring (designated as D), there exists a diffraction ring inside the diamond ring, representing the Au phase. The intensity of Au ring is stronger than the diamond one, implying that the Au nanoparticles are more abundant than the diamond in this region. Moreover, there exists a diffused ring at the center of FT_{0b} image, which corresponds to sp^2-bonded carbon. The ft_1-image corresponding to the region 1 highlights the presence of diamond phase, whereas the ft_2-image

corresponding to the region 2 highlights the existence of Au nanoparticles. In between the

diamond and Au nano-particulates, there present nanographitic phase, which is highlighted by

ft_3-image, corresponding to the region 3. Notably, for each of the Au nanoparticles, there are

graphitic phases encasing them, which are illustrated by the ft_4 image corresponding to the

region 4. Moreover, the cross-sectional HRTEM image of the interfacial layer (designated as B,

Fig. 2(a)) is shown in Fig. 2(c). The FT image of the whole structure image (FT_{0c}) shows that the

spotted diffraction pattern was arranged in a ring, which corresponds to Au phase. The existence

of diamond nuclei is revealed by the diffraction spots located outside the Au diffraction ring

(designated as D), whereas the presence of SiC phases is indicated by the diffraction spots

located inside the Au diffraction ring (designated as SiC). The presence of Si, diamond, Au and

SiC in these regions are highlighted by region 5 (ft_5), region 6 (ft_6), region 7 (ft_7) and region 8

(ft_8), respectively. The interaction of Au-coating with the diamond and Si in the interaction

region will be further examined using STEM and EELS analyses shortly.

The enhanced transport efficiency for electrons crossing the diamond-to-Si interface is also

a major factor resulting in superior EFE and PI behaviors for Au-UNCD/Au(Si) materials,

besides the high conductivity of the materials. The understanding on how the Au-coating

improves these behaviors is very important. For this purpose, the elemental distribution crossing

the interface in Au-UNCD/Au(Si) materials was analyzed using energy dispersive x-ray analysis

(EDX) in scanning TEM (STEM) mode. The STEM image is shown in Fig. 3(a), whereas the C,

Au, Cr, Pt, O and Si line profiles for the locations designated in the STEM are shown in Fig.

3(b). The carbon species are mainly located in regions I and II, whereas the Si species are placed

in region IV. In contrast, the Au species are present in regions I and III. The Au species in region

I exhibits a broad peak, due to the presence of implanted Au ions co-existing with the diamond, whereas those reside in regions III (the interfacial layer) shows a narrow peak, which is formed by the interaction of Au with Si substrate. The STEM image and EDAX profiles are in good agreement with the SIMS results shown in Fig. 1(a). There are also existence of Cr, Pt and O elements with very low intensities, which are either undercoating for Au layer or native oxide, and do not possess any significant role in this hybrid material. Furthermore, it is observed that the Si species diffused markedly through the interfacial layer outward to the diamond, but the C species that diffused inward towards the interfacial layer was less pronounced. Apparently, the outward diffusion of Si through the interfacial layer is much easier than the inward diffusion of C into the interfacial layer, as the interfacial layer is actually a Au-rich Au-Si eutectic layer.

To illustrate more clearly the elemental distribution of the species near the interface in Au-UNCD/Au(Si) hybrid materials, high-angle annular dark-field (HAADF) images in STEM mode using an HAADF detector with different camera lengths (CLs) were acquired and then superimposed. Markedly, in TEM, when the elastically scattered electrons were diffracted incoherently, the scattering angle is closely related to the atomic number of the species involved. The heavier the species are, the larger the scattering angle. An HAADF image, which provides information on the elemental distribution of the samples,[29,30] is obtained when the incoherently scattered electrons are collected by a high-angle annular detector. Fig. 3(c) shows a micrograph, composing of the HAADF images with Si (yellow; CL=93.3mm), Au (pink; CL=127.3mm), and C (black; CL=400.0mm). This figure indicates, again, that the Au species are present in the surface and the interface regions of the materials, which are due to Au-ion implantation and Au-interlayer coating, respectively. The diffusion of Si through interlayer (region III) toward

diamond (region II), forming SiC by reacting with C is clearly illustrated. There is no *a-C* phase

observable in the interlayer of Au-UNCD/Au(Si) materials.

The selective area carbon K-edge core-loss electron energy loss spectroscopy (EELS)

spectra for the selected regions in the Au-UNCD/Au(Si) materials (designated as dashed squares

in Fig. 3(a)) are shown in Fig. 4(a). The core-loss EELS corresponding to entire region in Fig.

3(a) is shown as curve 0 in Fig. 4(a), which indicates that, besides an abrupt rise at 289.5 eV

representing σ^*-band, there is a dip in the vicinity of 302 eV representing second diamond gap

and a small hump at 284.5 eV representing π^*-band. The plasmon-loss EELS spectrum for this

region is shown as curve 0 in Fig. 4(b), which contains s_2-band at 23 eV and s_4-band at 33 eV

peaks with s_2/s_4 intensity ratio much larger than $1/\sqrt{2}$, implying that the plasmon-loss EELS

contains a diffuse peak near 27 eV (s_3 peak). These core-loss and plasmon-loss EELS spectra

mark the coexistence of graphitic phase with the diamond in the entire region corresponding to

Fig. 3(a).[31,32] Particularly, the plasmon-loss EELS spectrum is an effective measurement for

distinguishing the crystalline *sp³*-bonded carbons (the diamond) and crystalline *sp²*-bonded

carbons (the graphite) from the amorphous *sp²*-bonded carbons, because the graphitic phase

shows a prominent peak at s_3 (27 eV) and the *a-C* phase shows a peak at s_1 (22 eV) in plasmon-

loss EELS spectrum ,[33,34] whereas the *sp³*-bonded carbon, the diamond, shows a peak at s_4 (33

eV) with a shoulder at s_2 (23 eV) and s_2/s_4 intensity ratio is around $1/\sqrt{2}$.[33,34] The inset in Fig.

4(a) shows the existence of a peak at 109 eV in the core-loss EELS spectrum, which corresponds

to SiC materials, confirming the presence of SiC phases in these materials.[35,36] The containment

of Si species in these materials is evidenced by the presence of a peak at 18 eV in plasmon-loss

EELS.[35,36] In contrast, the core-loss EELS corresponding to region *i* in Fig. 3(a) also contains σ^*-

band (~289.5 eV) and a dip (~302 eV), but with essentially no π*-band at 285 eV, whereas the

plasmon-loss EELS spectrum for this region shown as curve i in Fig. 4(b) contains s_2 and s_4

peaks with s_2/s_4 intensity ratio close to $1/\sqrt{2}$. This is an indication that this region is

predominated with diamond and there is very small amount of sp^2-bonded carbon contained in

this region.[33]

Curve iii in Fig. 4(a) shows the carbon core-loss EELS spectrum corresponding to region

iii in Fig. 3(a), which illustrates that this region is predominated with sp^2-bonded carbon, as this

spectrum contains a large hump at 285 eV. The signature for diamond materials (i.e., the σ*-

band and the dip) is too weak to be observable. Better understanding from the plasmon-loss

EELS spectrum corresponding to this region (curve iii, Fig. 4(b)) reveals that there appears a

peak at 27 eV corresponding to crystalline sp^2-bonded carbon which confirms that there is a

conversion of diamond into graphitic phases due to Au-ion implantation in this region. A peak at

62 eV in the core-loss EELS spectrum, which corresponds to Au materials, confirms the

presence of Au nanoparticles in the region *iii* of the materials (inset of Fig. 4(b)). Moreover, a

detailed analysis of regions *ii* and *iv* using EELS reveals that the UNCD materials in these

regions were also converted into sp^2-graphitic phases due to ion-implantation (curves ii and iv in

Fig. 4(a) and (b)), respectively). The TEM-EELS observations confirm that the Au-

UNCD/Au(Si) hybrid structured materials are composed of layers of UNCD and Au-diamond

hybrid materials, co-existing with some proportion of nanographitic phases.

For a good electron field emitter, sufficient electrons supply from the substrates (the Si) to

the emitting sites (the diamond) is critical, besides the low work function for the emitting

surface. For enhancing the efficiency for the supply of electrons, both the conductivity of the diamond and the resistance of diamond-to-Si interface need to be optimized. The utilization of Au species, which were either implanted into the UNCD materials or were precoated on Si substrates prior to the growth of UNCD materials, fulfills the two critical requirements simultaneously, as TEM investigations illustrated that, in the surface region of Au-UNCD/Au(Si) materials, the Au-ions implanted into the UNCD materials form Au nanoparticles, which induce nanographitic phases and improving the conductivity of the films. In contrast, in the interface region, suppressing the formation of *a-C* phase and enhancing the transport of electrons crossing the interface. Nevertheless, there remains some unresolved questions of what is the role of Au species in (i) enhancing the nucleation of diamond in the vicinity of diamond-to-Si interface region and (ii) forming the nanographite phase in the bulk of Au-UNCD/Au(Si) hybrid structured materials. The formation mechanism for ultra-small grains in conventional UNCD materials grown in CH_4/Ar plasma could be due to the presence of large proportion of C_2[38] or CH_3 and other C_1 radicals[39,40] in the plasma, as these species re-nucleate easily, forming diamond cluster on Si substrates. However, the nucleation of these active carbonaceous species on Si surface is still very difficult and usually requires the formation of an *a-C* layer.[41,42] In the present study, due to the formation of Au-Si eutectic interlayer, the active Si species, which diffused easily through the interfacial layer, are in atomic form and are very active. They can react with the active C_2 species in the gas chemistry instantaneously, forming SiC clusters. The presence of Au layer might also play an important role in catalyzing the formation of SiC clusters.[43] The SiC nanoclusters are isostructure with diamond and can trigger the nucleation of the diamond cluster without the necessity of forming an *a-C* layer.

14

On the other hand, the explanation on the role of Au-species implanted into UNCD materials in inducing the formation of nano-structured hybrid materials is more complicated. Various groups have highlighted the role of nano-metallic particles in catalytic inducing the growth of nanocarbon materials.[44–46] It has been demonstrated that the nanosized Au particles have some carbon solubility,[16,17,47] which can catalytically induce the formation of carbon nanowire or a SWNT, depending on the catalyst particle size. Moreover, Au species have been observed to catalytically convert the CH species (*trans*-polyacetylene phases) in the gas chemistry into nanographitic phases.[48–51] These phenomena provide some insight into the mechanism of the phase transformation process occurred in Au-UNCD/Au(Si) materials, viz., the implanted Au-species first formed nano-sized Au-particles, which catalytically converted the grain boundary phase and even the nano-size diamond grains into nanographitic clusters.

Consequently, the enhancement in the EFE and the PI properties of conducting Au-UNCD/Au(Si) hybrid structured materials is believed to be due the non-occurrence of *a-C* phase in the interfacial region and the induction of nanographitic clusters in the ion implanted region. The former lowered the resistivity of the interfacial layer, whereas the latter increased markedly the conductivity of the materials. Therefore, the electrons can be transferred effortlessly from Si substrates across the interfacial layer to the diamond region due to the utilization of Au-Si eutectic layer. Once the electrons can pass through diamond-to-Si interface easily, they can transport easily through the nanographitic phases induced due to Au-ion implantation to the emitting surface and are then emitted to vacuum without any difficulty as the diamond surfaces are NEA in nature.[52,53]

In summary, a facile and reproducible way of fabricating Au-UNCD/Au(Si) hybrid structured materials with excellent EFE and PI performances is being demonstrated. The Au-nanoparticles hybridized in the UNCD materials markedly enhance the electrical conductivity (230 $(\Omega \text{ cm})^{-1}$) and the EFE properties (viz. low turn-on field of 2.1 V/μm with high EFE current density of 5.3 mA/cm^2 at 4.9 V/μm) of the hybrid materials. Such an enhancement in the conductivity/field emission behavior originates from the unique materials combination. The Au nanoparticles formed from implanted Au-ions catalytically induced the formation of nanographitic phases encasing the Au nanoparticles that lead to the betterment of the conductivity for the materials. Moreover, the formation of Au-Si eutectic layers due to Au-coating induces the formation of SiC clusters in the interface, eliminating the formation of *a-C* phase via efficiently nucleating the diamond and improving the transport of electrons crossing the diamond-to-Si interface. Both factors result in the enhanced EFE properties of UNCD materials. The potential application of these materials is demonstrated by the PI measurements for a microplasma devices, that is, the lowering of the threshold voltage by 350 V and the increase in plasma density to n_p=1.5 x 10^{17} cm^{-3}. These observations confirmed the role of Au in the enhancement of electron emission behavior of Au-UNCD/Au(Si) hybrid structured materials. Consequently, the present approach for fabricating Au-UNCD/Au(Si) hybrid structured materials is a simple and a direct process that opens new prospects in flat panel displays and high brightness electron sources.

Experimental Section

UNCD materials were grown on *n*-type silicon substrates by microwave plasma enhanced chemical vapor deposition (MPECVD; 2.45 GHz, 6″ IPLAS-CYRANNUS-I, Troisdorf,

Germany) system, using Ar(99%)/CH$_4$(1%) gas at 1200 W and 120 Torr. Si substrates were cleaned with sulfuric acid/hydrogen peroxide and ammonia/hydrogen peroxide mixtures, respectively. Prior to the growth of UNCD materials, a 5 nm Cr and a 100 nm Au were subsequently deposited on Si substrates by dc sputter deposition system (Helix Co., Taiwan) using a power of 50 W in Ar partial pressure of 5 mTorr. The purpose of Cr layer was to achieve strong adhesion of Au on Si. The Au-coated Si substrates were then ultrasonicated for 45 min in methanol solution containing the mixture of nanodiamond powder (about 4 nm in size) and titanium powder (SIGMA-ALDRICH) (365 mesh) to facilitate the nucleation process. The growth process of UNCD materials on Au-coated Si substrates was carried out without any intentional heating of the substrate. The low growth temperature of <475 °C was estimated with a thermocouple attached to the substrate holder. It should be noted that such a growth temperature was higher than that of the Au-Si eutectic temperature (363°C). Therefore, it is expected that the Au-coating will interact with the Si substrates eutectically resulting in an Au-layer enriched in Si (~19%) as soon as the substrates were heated up over the eutectic point due to plasma ion bombardment. The Si substrate with Au-Si eutectic compound as interlayer was designated as Au(Si). The UNCD materials were grown on the Au(Si) substrates for 360 min to reach a thickness of 800 nm, which was confirmed from the cross-sectional field emission scanning electron microscopy (JEOL 6500) image (figure not shown). Finally, 500 keV Au ions with an ion fluence of 1 x 10^{17} ions/cm^2 and ion flux of 1.035 x 10^{12} ions/cm^2/s were implanted on UNCD materials at room temperature in a pressure below 10^{-7} Torr and the obtained materials are designated as "Au-UNCD/Au(Si)" hybrid structured materials.

The depth profiles of these hybrid structured materials were characterized by secondary ions mass spectroscopy (SIMS, Cameca IMS-4f). The detailed microstructure and bonding structure of the samples were examined using EELS (Gatan Enfina) in TEM (Jeol 2100F). Hall measurements were carried out in a van der Pauw configuration (ECOPIA HMS-3000) to examine the conducting behavior of these hybrid materials. To investigate the effect of interfacial characteristics on the transport behavior of electrons, the electrical resistivity of the hybrid materials were measured by a four-probe technique, in which, two configurations were utilized: (i) with all 4 probes located on the surface of the materials for measuring the resistivity along the film surface (inset of Fig. 1(b)) and (ii) with 2 of the probes located on the UNCD film surface and the other 2 probes located on the UNCD-to-Si interface for measuring the resistivity through the film thickness (inset of Fig. 1(c)). The EFE properties of the samples were measured with a tunable parallel plate setup, in which the cathode (Au-UNCD/Au(Si))-to-anode (molybdenum rod with a diameter of 2 mm) distance was controlled using a micrometer. The current-voltage (I-V) characteristics were measured using an electrometer (Keithley 2410) under pressure below 10^{-6} Torr (1.3×10^{-4} Pa).

The PI characteristics of a microcavity were also investigated, in which an indium tin oxide (ITO)-coated glass was used as anode and the Au-UNCD/Au(Si) hybrid structured materials were used as cathode. The cathode-to-anode separation was fixed by a polytetrafluoroethylene (PTFE) spacer (1.0 mm in thickness). A circular hole about 6.0 mm in diameter was cut out from the spacer (PTFE) to shape a microcavity. The chamber was evacuated to reach a base pressure of 0.1 mTorr (13 mPa) and then purged with Ar for 10 min. The Ar gas was flowed into the chamber at a flow rate of 10 sccm throughout the measurements. The plasma was triggered using

18

a pulsed direct current voltage in a bipolar pulse mode (20 ms square pulse, 6 kHz repetition rate) at 12 Torr (1599 Pa). The plasma current versus applied voltage behavior was measured using an electrometer (Keithley 237).

Acknowledgements

References

1 R. Jiang, B. Li, C. Fang and J. Wang, *Adv. Mater.*, 2014, **26**, 5274−5309.

2 L. Nicole, C. L. Robert, L. Rozes and C. Sanchez, *Nanoscale*, 2014, **6**, 6267−6292.

3 R. B. Jiang, H. J. Chen, L. Shao, Q. Li and J. F. Wang, *Adv. Mater.*, 2012, **24**, OP200−OP207.

4 W. Schartl, *Nanoscale*, 2010, **2**, 829−843.

5 S. N. Kim, J. M. Slocik and R. R. Naik, *Small*, 2010, **6**, 1992−1995.

6 D. J. Guo and H. L. Li, *Carbon,* 2005, **43**, 1259−1264.

7 L. Dai, D. W. Chang, J. B. Baek and W. Lu, *Small*, 2012, **8**, 1130−1166.

8 M. Haruta and M. Date, *Applied Catalysis A*, 2001, **222**, 427−437.

9 B. Hvolbaek, T. V. W. Janssens, B. S. Clausen, H. Falsig, C. H. Christensen and J. K. Norkov, *Nano Today,* 2007, **2,** 14−18.

10 M. Veres, E. Perevedenstseva, A. V. Karmenyan, S. Totha dn M. Koos, *phys. status solidi C,* 2010, **7**, 1211−1214.

11 J. Jia, K. Haraki, J. N. Kondo, K. Domen and K. Tamaru, *J. Phys. Chem. B,* 2000, **104**, 11153–11156.

12 W. Wu, L. Liao, S. Zhang, J. Zhou, X. Xiao, F. Ren, L. Sun, Z. Dai and C. Jiang, *Nanoscale*, 2013, **5**, 5628–5636.

13 X. F. Duan and C. M. Lieber, *Adv. Mater.,* 2000, **12**, 298–302.

14 S. Bhaviripudi, E. Mile, S. A. Steiner, A. T. Zare, M. S. Dresselhaus, A. M. Belcher and J. Kong, *J. Am. Chem. Soc.,* 2007, **129**, 1516–1517.

15 T. Oznuluer, E. Pince, E. O. Polat, O. Balci, O. Salihoglu and C. Kocabas, *Appl. Phys. Lett.*, 2011, **98**, 183101.

16 N. Yoshihara, H. Ago and M. Tsuji, *Jpn. J. Appl. Phys.*, 2008, **47**, 1944–1948.

17 M. Valden, X. Lai and D.W. Goodman, *Science*, 1998, **281**, 1647–1650.

18 N. D. Skelland and P. D. Townsend, *J. Phys. D: Appl. Phys.*, 1994, **27**, 1672–1677.

19 X. J. Hu, J. S. Ye, H. J. Liu, Y. G. Shen, X. H. Chen and H. Hu, *J. Appl. Phys.*, 2011, **109**, 053524.

20 X. J. Hu, J. S. Ye, H. Hu, X. H. Chen and Y. G. Shen, *Appl. Phys. Lett.*, 2011, **99**, 131902.

21 K. J. Sankaran, K. Panda, B. Sundaravel, N. H. Tai, and I. N. Lin, *J. Appl. Phys.*, 2014, **115**, 063701.

22 K. J. Sankaran, K. Panda, B. Sundaravel, N. H. Tai, and I. N. Lin, J. Mater. Chem. C, (2015) in press.

23 K. J. Sankaran, H. C. Chen, C. Y. Lee, N. H. Tai and I. N. Lin, *Appl. Phys. Lett.*, 2013, **102**, 061604.

24 R. H. Fowler and L. Nordheim, *Proc. R. Soc. London, Ser. A*, 1928, **119**, 173−181.

25 J. G. Eden, S. J. Park, N. P. Ostrom, S. T. McCain, C. J. Wagner, B. A. Vojak, J. Chen, C. Liu, P. von Allmen, F. Zenhausern, D. J. Sadler, C. Jensen, D. L. Wilcox and J. J. Ewing, *J. Phys. D: Appl. Phys.*, 2003, **36**, 2869−2877.

26 S. Zhang, C. Gu and H. Xu, *Small*, 2014, **10**, 4264−4269.

27 A. Stacey, S. Prawer, S. Rubanov, R. Ahkvlediani, S. Michaelson and A. Hoffman, *Appl. Phys. Lett.*, 2009, **95**, 262109.

28 S. Kunuku, K. J. Sankaran, C. Dong, N. H. Tai, K. C. Leou and I. N. Lin, *RSC Advances*, 2014, **4**, 47865−47875.

29 P. A. Midgley and M. Weyland, *Ultramicroscopy*, 2003, **96**, 413−431.

30 S. Bals, G. Van Tendeloo and C. Kisielowski, *Adv. Mater.*, 2006, **18**, 892−895.

31 R. Arenal, P. Bruno, D. J. Miller, M. Bleuel, J. Lal and D. M. Gruen, *Phys. Rev. B*, 2007, **75**, 195431.

32 D. M. Gruen, S. Liu, A. R. Krauss, J. Luo and X. Pan, *Appl. Phys. Lett.*, 1994, **64(12)**, 502−1504.

33 P. Kovarik, E. B. D. Bourdon and R. H. Prince, *Phys. Rev. B*, 1993, **48**, 12123.

34 S. Prawer, J. L. Peng, J. O. Orwa, J. C. McCallum, D. N. Jamieson and L. A. Bursill, *Phys. Rev. B*, 2000, **62**, R16360.

35 W. M. Skiff, R. W. Carpenter and S. H. Lin, *J. Appl. Phys.*, 1987, **62**, 2439−2449.

36 R. Schneidery, J. Woltersdorfy and O. Lichtenberger, *J. Phys. D: Appl. Phys.*, 1996, **29**, 1709−1715.

37 A. Politano and G. Chiarello, *Gold Bulletin*, 2009, **42**, 195−200.

38 D. Zhou, T. G. McCauley, L. C. Qin, A. R. Krauss, and D. M. Gruen, *J. Appl. Phys.*, 1998, *83*, 540−543.

39 P. W. May, Y. A. Mankelevich, J. N. Harvey and J. A. Smith, *J. Appl. Phys.*, 2006, **99**, 04907.

40 J. R. Rabeau, P. John, J. I. B. Wilson and Y. Fan, *J. Appl. Phys.*, 2004, **96**, 6724−6732.

41 K. J. Sankaran, K. Panda, B. Sundaravel, H. C. Chen, I. N. Lin, C. Y. Lee and N. H. Tai, *ACS Appl. Mater. Interfaces*, 2012, **4**, 4169−4176.

42 H. C. Chen, K. J. Sankaran, S. C. Lo, L. J. Lin, N. H. Tai, C. Y. Lee and I. N. Lin, *J. Appl. Phys.*, 2012, **112**, 103711.

43 S. H. Nam, M. H. Kim, J. S. Hyun, Y. D. Kim and J. H. Boo, *J. Nanosci. Nanotech.*, 2010, **10**, 2741−2745.

44 S. Y. Lee, M. Yamada and M. Miyake, *Carbon,* 2005, **43**, 2654−2663.

45 L. Sun, J. Gong, D. Zu, Z. Zhu and S. He, *Adv. Mater.*, 2004, **16**, 1849−1853.

46 Y. Li, W. Kim, Y. Zhang, M. Rolandi, D. Wang and H. Dai, *J. Phys. Chem. B***,** 2001, **105**, 11424−11431.

47 D. Takagi, Y. Kobayashi, H. Hibino, S. Suzuki and Y. Homma, *Nano let.,* 2008, **8**, 832−835.

48 A. Oya and S. Otani, *Carbon*, 1979, **17**, 131−137.

49 W. Lu, K. Komvopoulos and S.W. Yeh, *J. Appl. Phys.*, 2001, **89**, 2422–2433.

50 K. Bewilogua, R. Wittorf, H. Thomsen and M. Weber, *Thin Solid Films*, 2004, **447**, 142–147.

51 Y. V. Pleskov, Y. E. Evstefeeva and A. M. Baranov, *Diamond Relat. Mater.*, 2002, **11**, 1518–1522.

52 H. Yamaguchi, T. Masuzawa, S. Nozue, Y. Kudo, I. Saito, J. Koe, M. Kudo, T. Yamada, Y. Takakuwa and K. Okano, *Phys. Rev. B*, 2009, **80**, 165321.

53 M. W. Geis, S. Deneault, K. E. Krohn, M. Marchant, T. M. Lyszczarz and D. L. Cooke, *Appl. Phys. Lett.*, 2005, **87**, 192115.

Table 1. Comparison on the electrical conductivity and the electron field emission properties of conducting UNCD materials

Materials	Electrical conductivity $(\Omega\,cm)^{-1}$	Turn-on field $(V/\mu m)$	EFE current density (mA/cm^2)
O-ion implanted UNCD/Si[19]	33.3	--	--
P-ion implanted UNCD/Si[20]	0.09	--	--
Cu-ion implanted UNCD/Si[21]	95.0	4.8	3.6 @ 8.0 V/μm
Pt-ion implanted UNCD/Si[22]	94.0	4.17	5.08@ 7.2 V/μm
Au-ion implanted UNCD/Si[23]	185	4.7	4.5 @ 8.1 V/μm

Au-UNCD/Au(Si) hybrid materials[This study]	230	2.6	5.3 @ 4.97 V/μm

Figure captions

Figure 1. (a) SIMS depth profiles of C, Au, and Si species in Au-UNCD/Au(Si) hybrid structured materials; (b, c) the electrical resistance (current-voltage curves) measured by four probes technique at atmospheric environment, where the current was either flowing (b) along the surface of the materials (i.e., with all four probes placed on the same surface of the materials, inset of Fig. 1(b)) or 1(c) across the UNCD-to-Si interface (i.e., with two of the probes on the surface of the diamond materials and two on the Si substrates, inset of Fig. 1(c)); (d) electron field emission properties (current density-applied field curves) and the current density versus time curves (inset of Fig. 1(e)) measured in high vacuum environment (the curve I is for UNCD/Si and the curve II is for Au-UNCD/Au(Si) hybrid materials in Fig. 1(b), 1(c) and 1(d)); (e) the plasma illumination images of the microplasma cavities fabricated using (I) UNCD/Si or (II) Au-UNCD/Au(Si) as cathode materials, (f) plasma density versus applied field of a microplasma cavity with inset showing the plasma illumination stability which utilized the ITO coated glass as anode and using either (I) UNCD/Si or (II) Au-UNCD/Au(Si) as cathode materials.

Figure 2. (a) Typical cross-sectional TEM micrograph with the inset showing the corresponding SAED pattern of Au-UNCD/Au(Si) hybrid materials; (b) and (c) HRTEM images, of Au-UNCD/Au(Si) hybrid materials, corresponding to the regions A and B of Fig. 2(a), respectively. The insets (FT_{0b} and FT_{0c}) show the Fourier-transformed images corresponding to the whole structure images in Fig. 2(b) and 2(c), respectively, whereas the ft_1 to ft_8 images show the FT images corresponding to regions 1 to 8, respectively.

Figure 3. (a) Cross-sectional STEM BF image of Au-UNCD/Au(Si) hybrid materials; (b) EDX linear scan with Si, Au, C, Cr, Pt and O elemental profiles, along the lines designated in Fig. 3(a); (c) HAADF images of the regions corresponding to Fig. 3(a).

Figure 4. Selective area the carbon edge (a) core-loss EELS spectra and (b) plasmon-loss EELS spectra corresponding to the entire region (curve 0) or regions *i* to *iv* (curves *i* to *iv*) of the cross-sectional STEM micrograph of Au-UNCD/Au(Si) hybrid materials shown in Fig. 3(a). The inset in Fig. 4(a) shows the core-loss EELS corresponding to SiC phase, whereas the inset in Fig. 4(b) shows the core-loss EELS corresponding to Au.
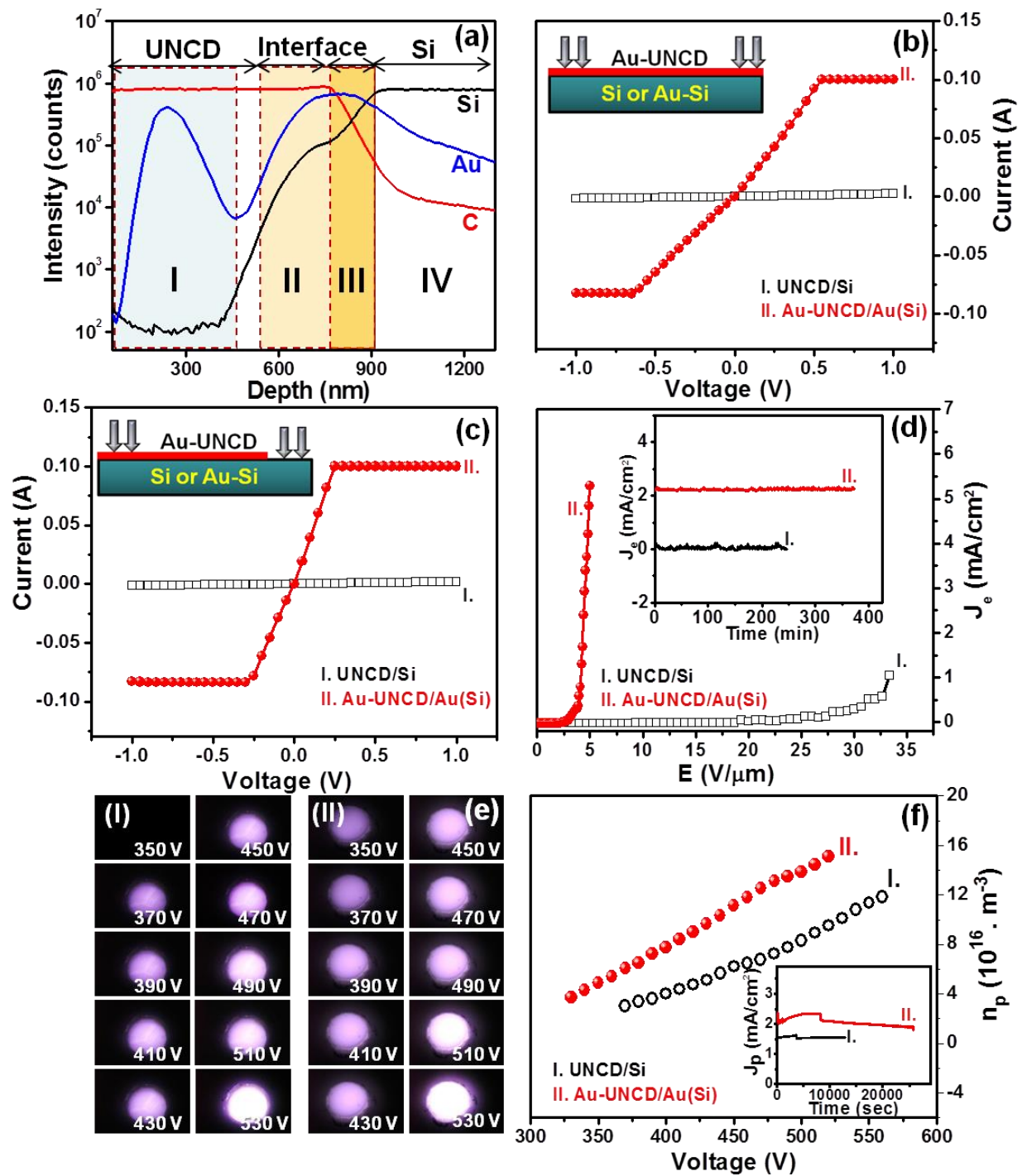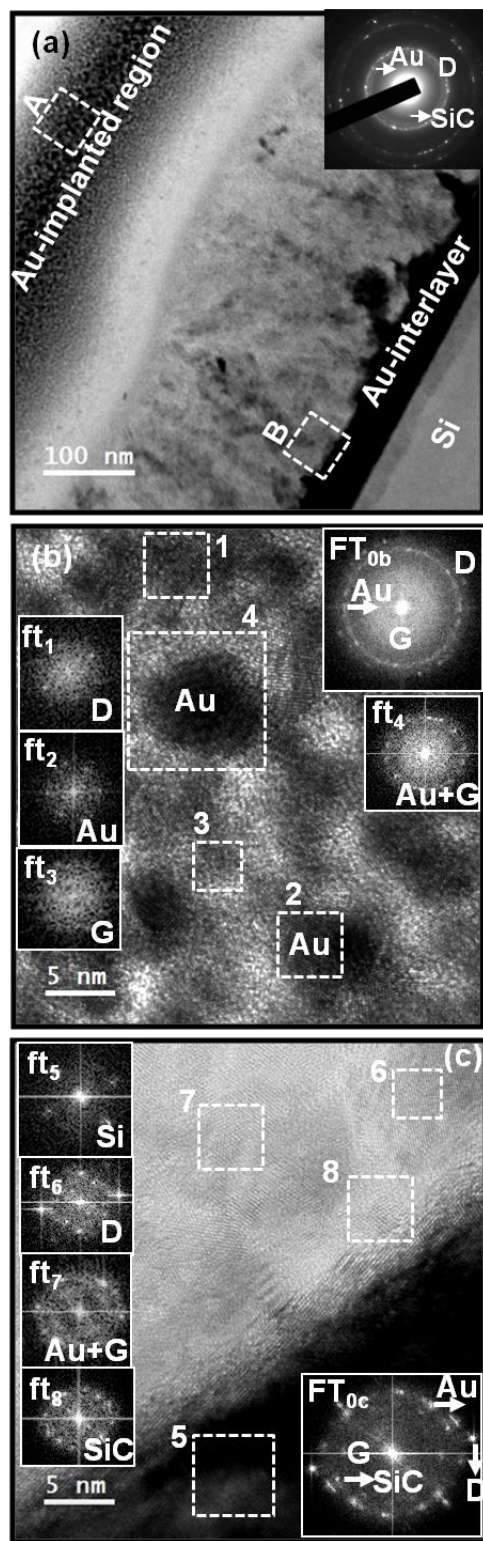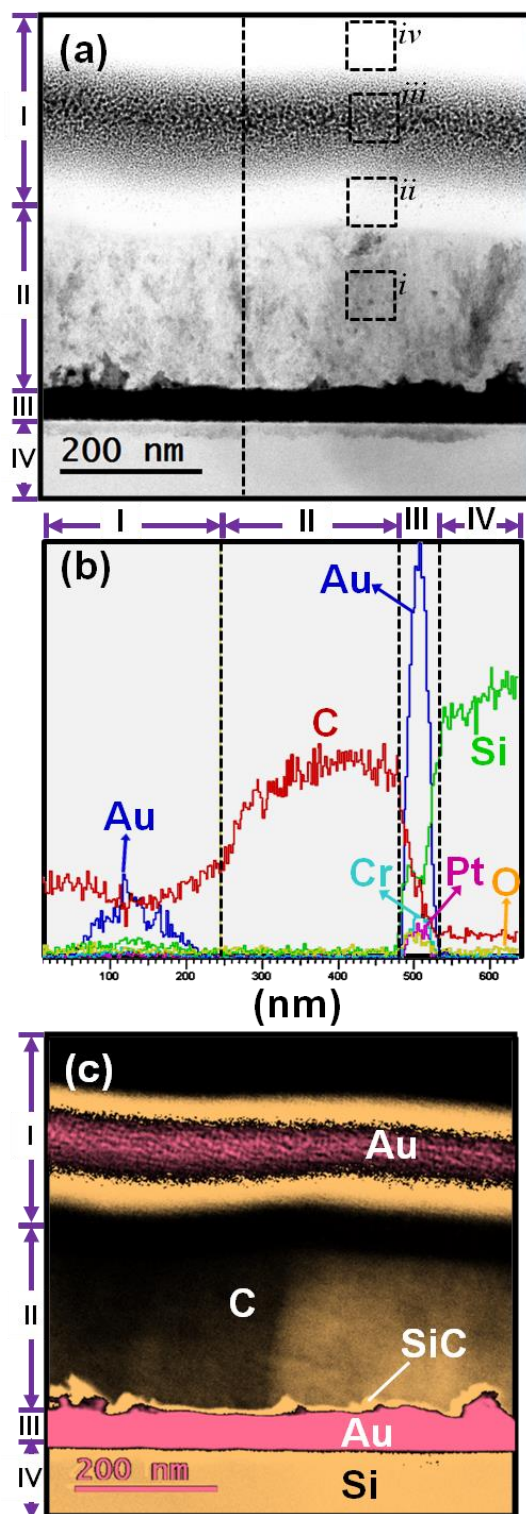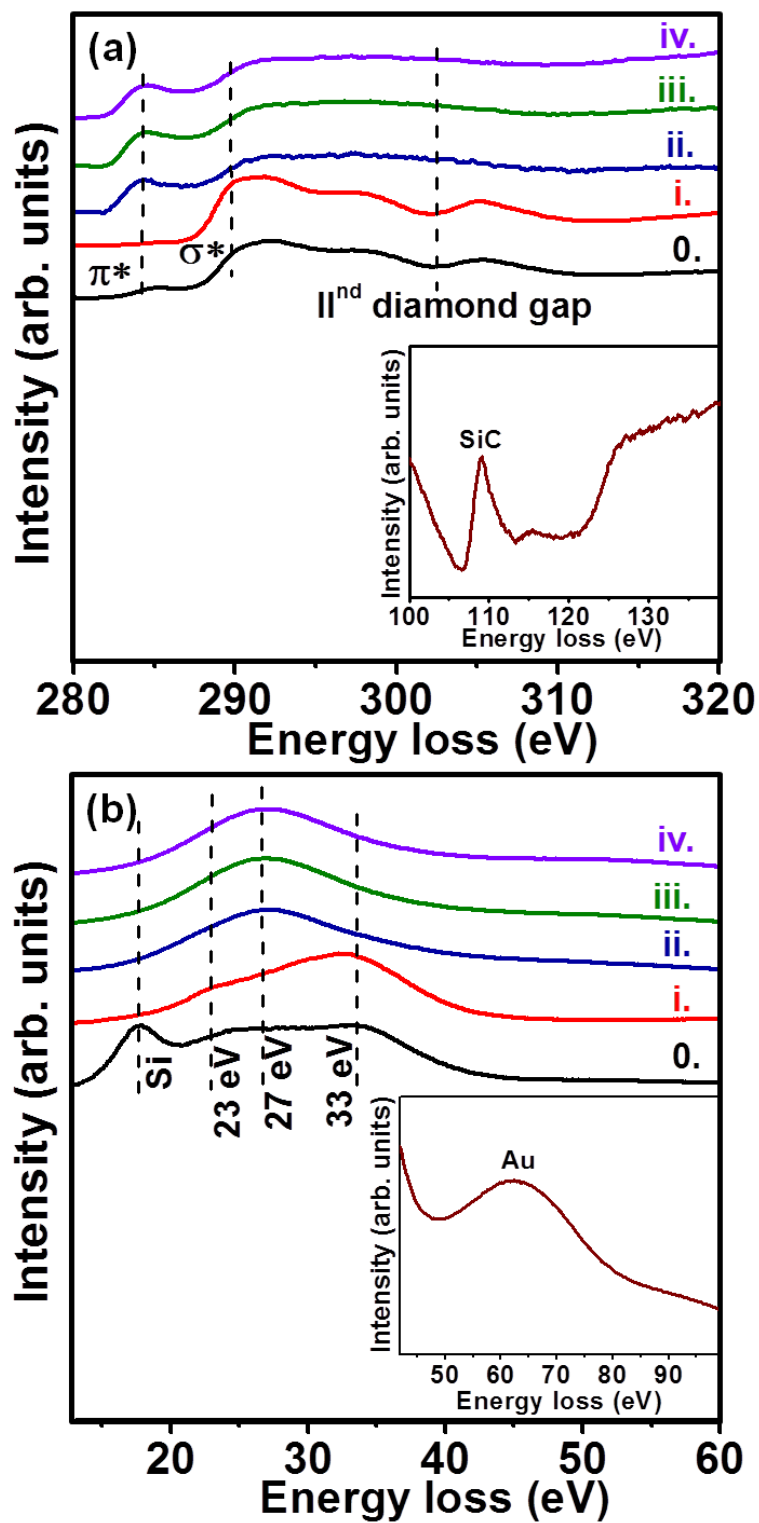
Figure 1.

Figure 2.

Figure 3.

Figure 4.